Phase I Final Report
For Contract F49620-98-C-0081

Micro-Cluster Propulsion for Nanosatellite Control

Prepared For:

Air Force Office of Scientific Research
Bolling AFB, DC 20332-8050

Period: 01 Sept 1998 - 28 Feb 1999

Principal Investigator: Dr. Julius Perel

ΨJ

Phrasor Scientific, Inc.
1536 Highland Ave.
Duarte, CA 91010
Phone: (626)357-3201
FAX: (626)357-3203

Subcontract: Professor Mark Cappelli
Thermosciences Division
Mechanical Engineering Department
Stanford University

REPORT DOCUMENTATION PAGE

AFRL-SR-BL-TR-99-

0178

1. AGENCY USE ONLY (Leave blank)	2. REPORT DATE 26 May 1999	3. REPORT TYPE AND DATES COVERED FINAL 01 Sep 1998–28 Feb 1999

4. TITLE AND SUBTITLE MICRO-CLUSTER PROPULSION FOR NANOSTELLITE CONTROL	5. FUNDING NUMBERS F49620-98-C-0081

6. AUTHOR(S)

Dr. Julius Perel, John F. Mahoney, Carl Sujo, Mark Cappelli

7. PERFORMING ORGANIZATION NAME(S) AND ADDRESS(ES) Phrasor Scientific, INc. 1536 Highland Avenue Duarte, CA 91010	8. PERFORMING ORGANIZATION REPORT NUMBER

9. SPONSORING / MONITORING AGENCY NAME(S) AND ADDRESS(ES) AFOSR/NA 801 North Randolph Street Arlington, VA 22203-1977	10. SPONSORING / MONITORING AGENCY REPORT NUMBER

11. SUPPLEMENTARY NOTES

12a. DISTRIBUTION / AVAILABILITY STATEMENT

DISTRIBUTION STATEMENT A
Approved for Public Release
Distribution Unlimited

12b. DISTRIBUTION CODE

13. ABSTRACT (Maximum 200 words)

Report developed under STTR contract. The purpose of the research, performed at Phrasor Scientific, Inc. and the Mechanical Engineering Department at Stanford University, described in this STTR Phase I final report was to demonstrate the feasibility of using charged microclusters as a suitable candidate for micro-electric propulsion showing compatibility for adaptation to microelectro-mechanical systems (MEMS) fabrication. The research was carried out to explore the electrohydrodynamic (EHD) emission properties of microclusters from single micro-capillaries using diagnostic techniques developed for measuring microthruster performance in terms of specific impulse and thrust. The program demonstrated that charged microclusters emission can occur from positive and negative voltages. A time-of-flight (TOF) data acquisition system was used to determine single micro-capillary emitter thruster performance. Specific impulses ≈ 300s were achieved with a corresponding thrust level of ≈ 1.25 μN. Research performed at Phrasor under another program reached Specific impulses of 500s. This thruster performance approaches levels which are acceptable for meeting AFOSR micro and nanospacecraft mission objectives once techniques are introduced for microfabricating arrays consisting of multiple micron-sized emitters. Propellant system emission studies also determined that higher levels of dopant along with lower flowrates will aid in the increase of charge-to-mass ratios in order to attain higher specific impulses.

14. SUBJECT TERMS Micropropulsion, Microspacecraft, Electricpropulsion, Microclusters, STTR Report	15. NUMBER OF PAGES 29
	16. PRICE CODE

17. SECURITY CLASSIFICATION OF REPORT Unclassified	18. SECURITY CLASSIFICATION OF THIS PAGE Unclassified	19. SECURITY CLASSIFICATION OF ABSTRACT Unclassified	20. LIMITATION OF ABSTRACT UL

Table Of Contents

1.0 Project Summary

The purpose of the research, performed at Phrasor Scientific, Inc. and the Mechanical Engineering Department at Stanford University, described in this STTR Phase I final report was to demonstrate the feasibility of using charged microclusters as a suitable candidate for micro-electric propulsion showing compatibility for adaptation to microelectro-mechanical systems (MEMS) fabrication. The research was carried out to explore the electrohydrodynamic (EHD) emission properties of microclusters from single micro-capillaries using diagnostic techniques developed for measuring microthruster performance in terms of specific impulse and thrust. The program demonstrated that charged microclusters emission can occur from positive and negative voltages. A time-of-flight (TOF) data acquisition system was used to determine single micro-capillary emitter thruster performance. Specific impulses ≈300s were achieved with a corresponding thrust level of ≈1.25 μN. Research performed at Phrasor under another program reached Specific impulses of 500s. This thruster performance approaches levels which are acceptable for meeting AFOSR micro and nanospacecraft mission objectives once techniques are introduced for microfabricating arrays consisting of multiple micron-sized emitters. Propellant system emission studies also determined that higher levels of dopant along with lower flowrates will aid in the increase of charge-to-mass ratios in order to attain higher specific impulses.

Innovative approaches for microfabricating multiple emitter arrays that exploit existing MEMS fabrication procedures were also examined on the program. The Phase I results, coupled with microcluster propulsion geometry being adaptive to MEMS micro-feature requirements, justify a Phase II continuation.

2.0 Introduction

This Phase I program addresses a candidate, low-cost micropropulsion technology for future batch-processed microspacecraft[1]. The novel technology described herein has the potential of fulfilling both military and commercial requirements to develop a suitable, miniaturized propulsion system for microspacecraft. Recently, propulsion options for microspacecraft were reviewed identifying colloid (hereafter called microcluster) thrusters as quite possibly the most suited for primary propulsion and attitude control[2]. Briefly, the innovative microelectric propulsion is based on the electrohydrodynamic (EHD) emission and acceleration of multiply charged microclusters. Compared with other electric propulsion options (ion, field-emission or Hall thrusters), microcluster propulsion technology appears most amenable to microfabrication techniques. Clearly new developments in microelectromechanical (MEMS) propulsion technology will be needed for microspacecraft systems since current technologies are either too cumbersome or susceptible to undesired complexity as miniaturization is introduced. Already technology has been demonstrated for batch-fabricating microstructures suitable for adaptation to microthruster designs.

Potential applications of the project results in Phase II include the unique mission opportunities made possible by deployment of microspacecraft constellations requiring attitude control and stationkeeping. Examples of multiple distributed microspacecraft applications are global surveys of planets which conserve fuel compared to single spacecraft operation. Commercially, microspacecraft powered by micro-electric propulsion systems are being proposed to provide global cellular telephone coverage, improved communication services (without terrestrial links) and low-cost message and position-relay services. Microspacecraft constellations are also envisioned for remote sensing commercial applications to manage crops, detect pollution and to aid meteorological observations for improved weather forecasting.

3.0 Program Tasks

The schedule shown in Fig. 1, taken from the proposal, lists the tasks planned for this program to demonstrate the feasibility of using micro-cluster emission and acceleration as a competitive candidate to develop a suitable, miniaturized propulsion system for some high delta-V maneuvers and attitude controls in microsatellites and nanosatellites. The aim of the program is to show appropriate size and emission characteristics of the electrohydrodynamic(EHD) method for ultimate production of MEMS type thrusters. This involves attaining direct thrust and specific impulse levels that are compatible with miniaturized thrusters for use with small potential nanosatellites. The work was performed by Perel, Mahoney, and Sujo at Phrasor Scientific, Inc. with subcontract work by Cappelli at Stanford University.

TASKS	Months After Contract Initiation						Staff Assigned
	1	2	3	4	5	6	
1. Fabricate and Evaluate Microcluster Sources at Phrasor Scientific Inc	▬	▬					J. Perel J. Mahoney
2. Thruster parameter measurements		▬	▬	▬			J. Perel C. Sujo
3. Fabricate and Deliver Microcluster Assemblies to Stanford Univ. for Quantitative Performance Evaluation	▬	▬	▬				J. Perel J. Mahoney C. Sujo
4. Direct particle velocimetry	▬	▬	▬				M. Cappelli
5. Direct thrust characterization			▬	▬	▬		M. Cappelli
6. Propellant system developement			▬	▬			J.Mahoney C.Sujo
7. MEM's design				▬	▬		J.Mahoney C.Sujo
8. Prepare final report						▬	J.Perel M. Cappelli J.Mahoney C.Sujo

Fig. 1

4.0 Description of Work Performed

4.1 Time-of-Flight (TOF) Analysis

4.1.1 TOF Micro-Emitter Data Acquisition System

The major parts of the TOF system that were used are shown in the flow diagram of Fig.2. Emission performance in terms of specific impulse, thrust, mass flowrate and mean charge-to-mass ratio of the emitted microclusters can be determined by analysis of the TOF waveforms. The TOF waveform is a current versus time trace which gives the current at the TOF collector at any time t, initiated when the DC emission is abruptly terminated by shorting the micro-emitter acceleration voltage to ground. The TOF switch shown in Fig.2 is used to accomplish the switching action (details of the TOF switch are given in Fig.3

below). A key requirement for the TOF switch design is that the switching time (the time it takes for the micro-emitter voltage to reach ground) be much less than the time taken for charged microclusters to reach the TOF collector. This is necessary to prevent TOF
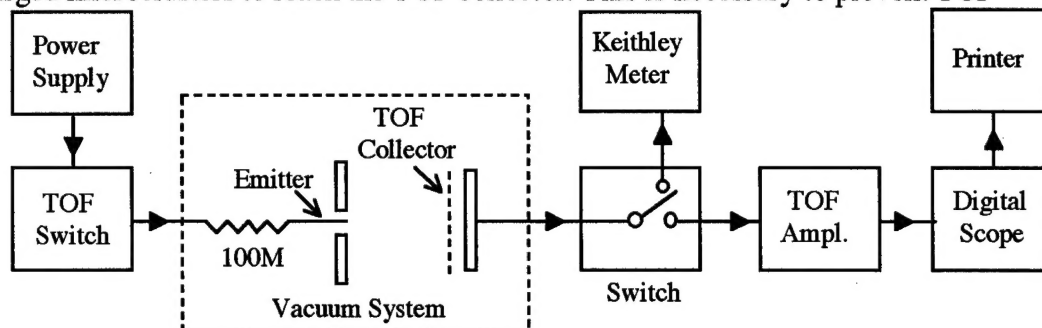

Fig. 2 Flow Diagram For Micro-Emitter TOF Diagnostic System

waveform distortion due to charged particle formation during the switching time. Another requirement is for the switch to exhibit bipolar operation so TOF waveform data can be acquired to evaluate micropropulsion performance for both negatively and positively charged microcluster beams. The switch design adopted, that fulfills these requirements, is shown in Fig 3. Switching occurs by magnetically actuating a mercury-wetted reed switch (Aleph International Part #900113540) consisting of a pair of flexible reeds made from a magnetic material. When a magnet is moved toward the reed switch mounted inside the switch box enclosure, the switch closes shorting the power supply voltage to ground initiating the TOF waveform.
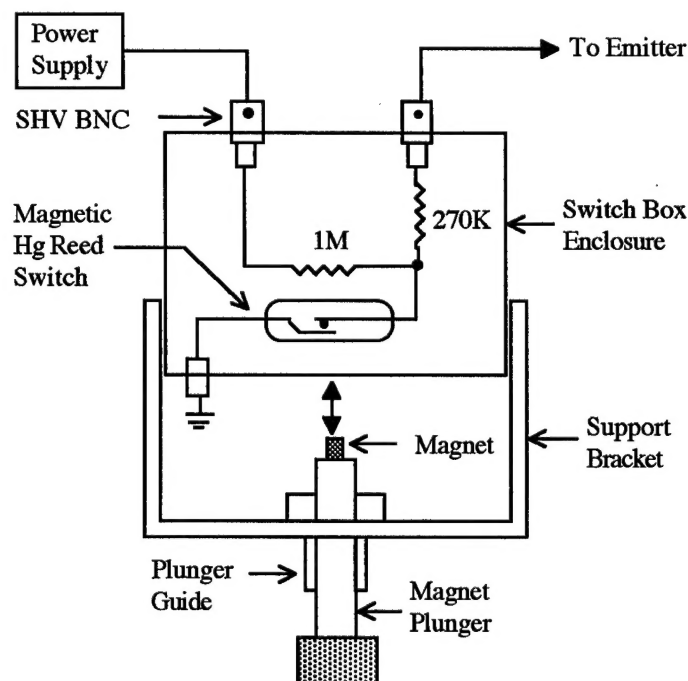

Fig. 3 Mercury-Wetted Magnetic Reed TOF Switch

Because emission currents in the range 0.1 to 10nA were anticipated for a single micro-emitter having orifice diameters of 5 micron, the output TOF collector current was

4

amplified prior to measurement at the horizontal input of the digital oscilloscope. Details of the TOF collector amplifier circuit with a calibrated gain factor of 10mV/nA is illustrated in
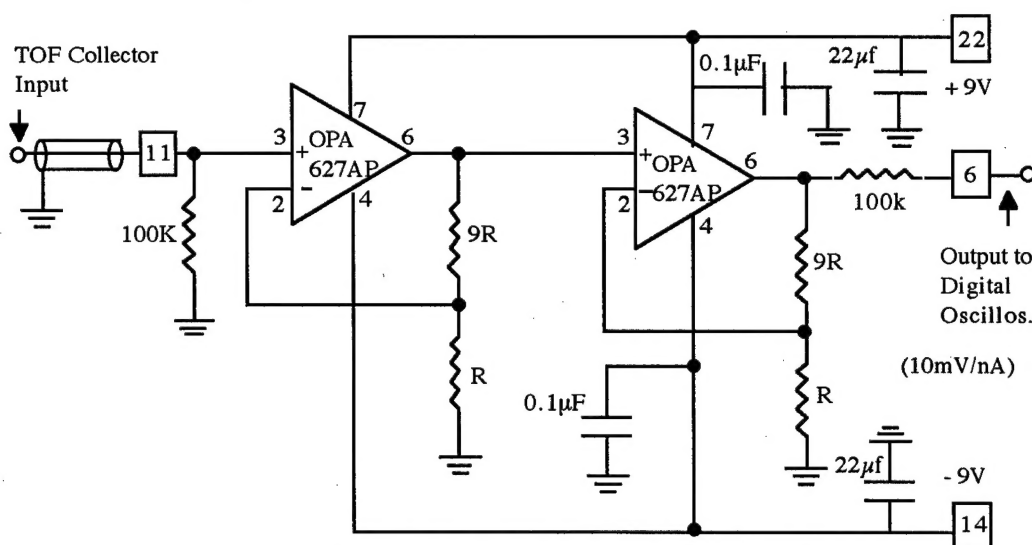

Fig.4 TOF Collector Amplifier Circuit

Fig.4. A shielded BNC switch box was inserted between the TOF collector and TOF amplifier to allow direct reading of collected micro-emitter currents using a Keithley 610C electrometer instrument. This feature permits periodic verification of the TOF amplifier performance and direct monitoring of the emission status of the micro-capillaries. The digital oscilloscope was equipped with a TDS2MM measurement extension module which provides a hard copy output recorded on an Epson stylus color 600 ink jet printer. A major improvement in the overall TOF data acquisition system shown in Fig.2 over past TOF systems is that the sensitivity of the present system has improved by a factor of 1000.

4.1.2   TOF Analysis of Positive and Negative Emission

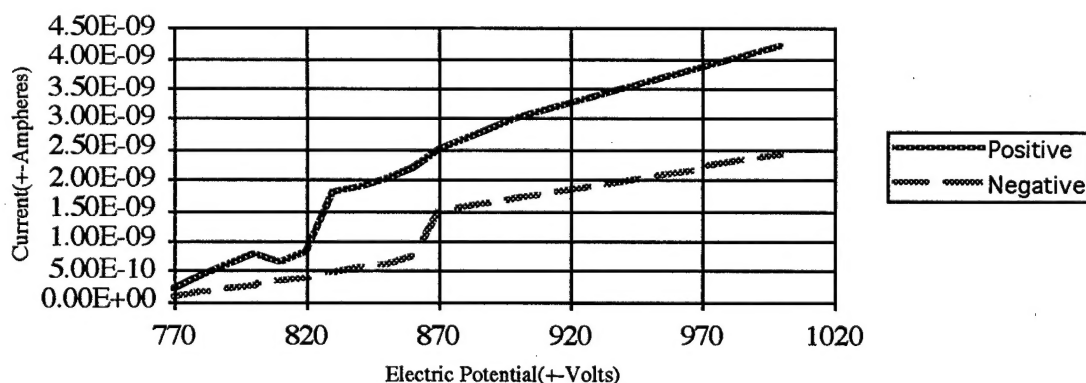I-V Characteristic of Positive and Negative Emission

Figure 5

5

Preceding the TOF analysis of Bipolar emission, Current-Voltage(I-V) characterization studies were done on positive and negative voltage. Bipolar emission is an important consideration for micropropulsion because it reaps the benefits of both thrust and neutralization of a nanosatellite without the need of a high power consuming electron emitter. Current-Voltage relationships were established by spraying 1.5M Ammonium Acetate in Glycerol solution from a 5 micron ID nozzle at high vacuum in the 10^{-5} torr range. Although not exact, the results indicated similar trends between positive and negative voltage. Greater positive and negative potential produced greater positive and negative current(Fig.5). Despite the greater negative voltage required to produce an equivalent current as the positive range, both do observe a similar jump in current at their own threshold points.
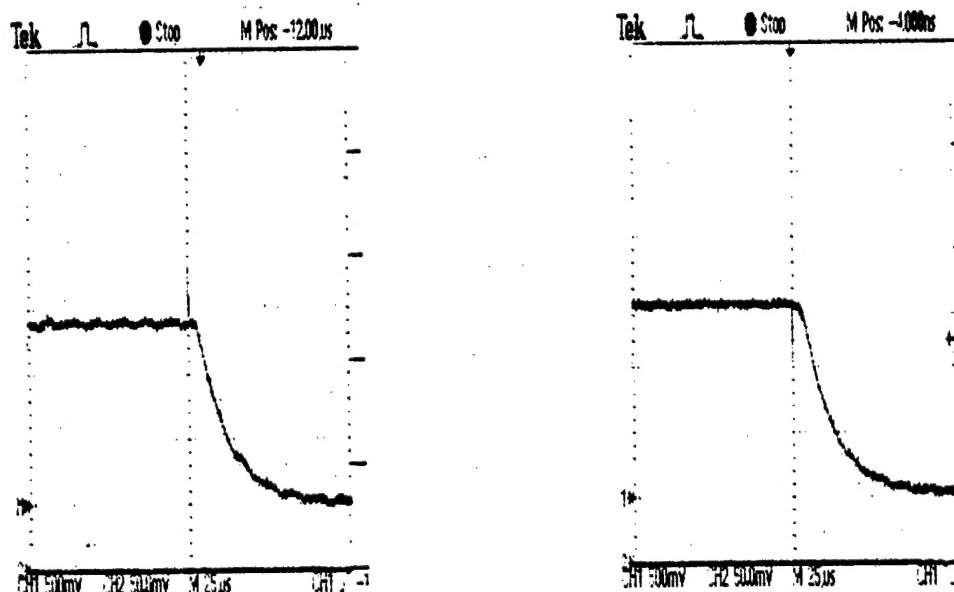
As described in section 2.1 and as illustrated in Fig. 2, the TOF diagnostic system was used to acquire current versus time waveforms of the microcluster beam for estimating micro-capillary thruster performance. Thruster performance was obtained from the TOF waveform data shown in Fig. 5a-b, for positive and negative emission using 1.3M NaI in glycerol. The acceleration voltages used to spray were +730V and -730V. At the present time, the math software necessary to automatically compute the area, A, under the TOF trace and the time coordinate of the TOF centroid, t_c, has not been acquired and integrated with the TOF data acquisition system.

The TOF waveforms seen in Fig. 6a-b were manually divided into equal time increments and numerically integrated to arrive at approximate values for A and t_c where

$$A = \Sigma\, i(t)\Delta t \tag{1}$$

and

$$t_c = (1/A)\,\Sigma\, t\, i(t)\Delta t \tag{2}$$

(a) +730V; 500 mV/div; 25 μs/div.   (b) -730 V; 500 mV/div; 25 μs/div.

Fig. 6.   TOF Waveforms of Positive and Negative Microcluster Beams

6

$$<q/m> = IL^2 / 4VA\, t_c \tag{3}$$

where I is the DC emission level of the micro-capillary (the waveform current at t = 0 before switching), L is the TOF distance and V is the applied micro-capillary voltage. The corresponding specific impulse is computed using

$$I_{sp} = L / 2gt_c \tag{4}$$

where g is acceleration due to gravity. The single micro-capillary thrust is given by

$$T = 2VA/L \tag{5}$$

This preliminary data with the 1.3M sodium iodide doped glycerol propellant indicates similar behavior when spraying with positive and negative voltage. Both $<q/m>$'s were found be approximately 300 C/kg, with I_{sp}'s at about 60 seconds, and T's at 0.035 μN. This confirms our belief that bipolar spraying works at low acceleration voltages.

4.1.3   Increasing Specific Impulse and Thrust

For the purposes of micro or nanosatellite propulsion, specific impulse and thrust must be high enough to meet requirements. These can be increased by raising the charge-to-mass ratio of the emission. From previous studies, it was determined that NaI solutions gave higher charge-to-mass ratios than Ammonium Acetate solution. Also, higher resistance in the flowrate of the propellant solution gave higher charge-to-mass ratios. This can be done by reconfiguring the nozzle type.

In order to raise the average charge-to-mass ratio of emission from a single 5 μm nozzle, several different emitter configurations were tested. These configurations were designed to raise electric field and/or reduce flowrate of the propellant. In order to increase electric field at the tip of the nozzle, the first design(see Fig.7) was a sharpened tip tungsten wire which came out of the tip of the glass nozzle. This was to allow propellant to flow out of the glass nozzle onto a sharp metallic tip, where a higher electric field can be generated and
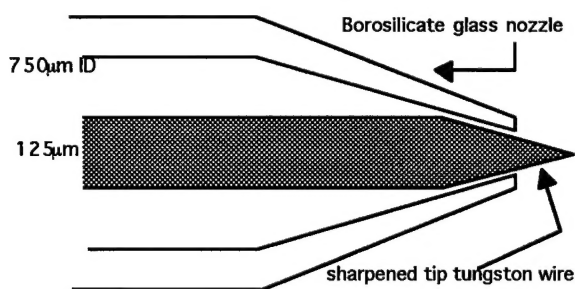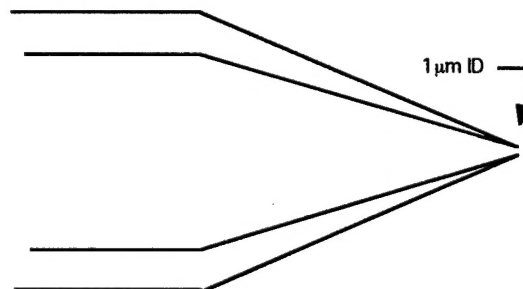

Fig. 7   Fig. 8

7

Beam

150 μm ID
Fused silica
Capillary

125μm
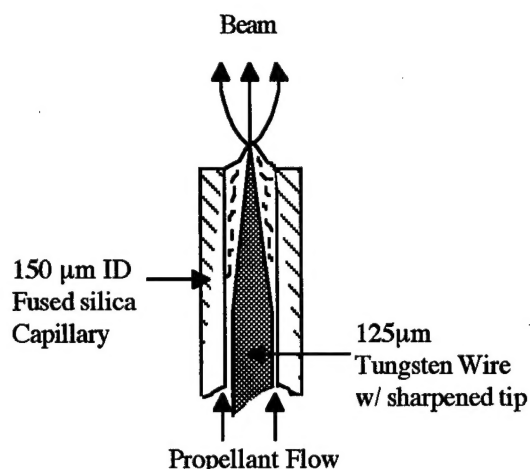Tungsten Wire
w/ sharpened tip

Propellant Flow

Fig. 9

sprayed. The second design(see Fig.8), a 1 μm tip nozzle, was chosen because of its smaller orifice. The smaller orifice increases the resistance to the propellant flow which reduces the flowrate. Also, the 1μm tip increases the electric field over the 5μm tip. The third design(see Fig.9), in order to reduce flowrate, uses a two inch long 150 μm ID fused silica. The resistance comes from the length of the fused silica. Also in the third design, to increase electric field, a 4.8 mil wire was sharpened and set up at the tip of the fused silica. The TOF diagnostic system was used to acquire current versus time waveforms of the microcluster beam for estimating micro-capillary thruster performance. Thruster performance was obtained from the TOF waveform data shown in Fig. 5a-c, for the three nozzle designs, using 1.3M NaI in glycerol. The acceleration voltages used to spray were +2200V, -620V, and +5400V respectively.

Using equations 1 thru 5, the TOF waveforms were analyzed to obtain $<q/m>$, Isp, and thrust.

Table 1. Summary Of Thruster Performance TOF Data

emitter	V (volts)	I (nA)	$<q/m>$ (C/kg)	I_{sp} (sec)	T (μN)	Fig.
Wire tip out of glass nozzle	+2200	640	247	92	2.32	2a
1 micron glass tip	-620	640	855	94	0.69	2b
Wire tip out of fused silica	+5400	740	1,790	309	1.25	2c

This data with the 1.3M sodium iodide doped glycerol propellant indicates that reduction of flowrate will help increase the $<q/m>$'s. Increasing resistance with the fused silica worked the best at increasing $<q/m>$'s as seen in Figure 10c and Table 1. However, a high voltage was required to generate a high enough electric field to spray at this level. Smaller orifices, such as 1 micron tips, require the least amount of voltage to generate a high electric field. This indicates that a 1 micron tip orifice on a high flow resistance emitter, such as 150 micron ID fused silica, may lead to higher $<q/m>$'s with low acceleration voltages.

8

(a) +2200V; 1 V/div; 25 μs/div.

(b) -620 V; 1 V/div; 25 μs/div.
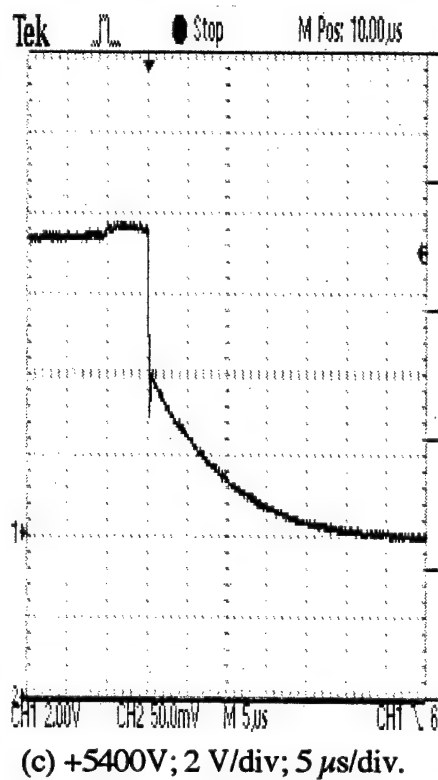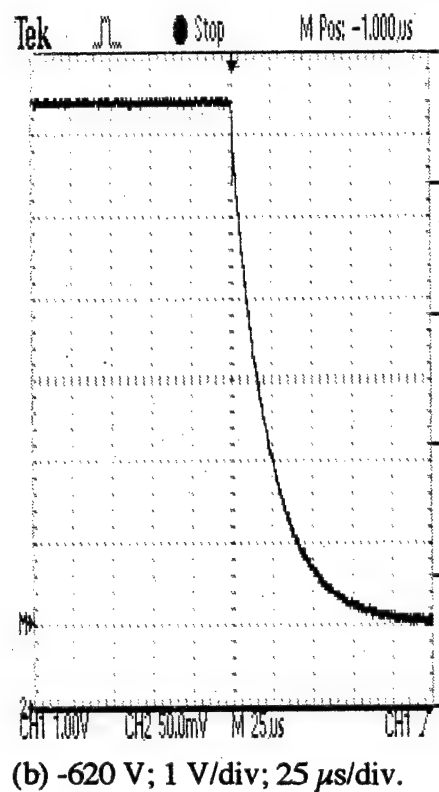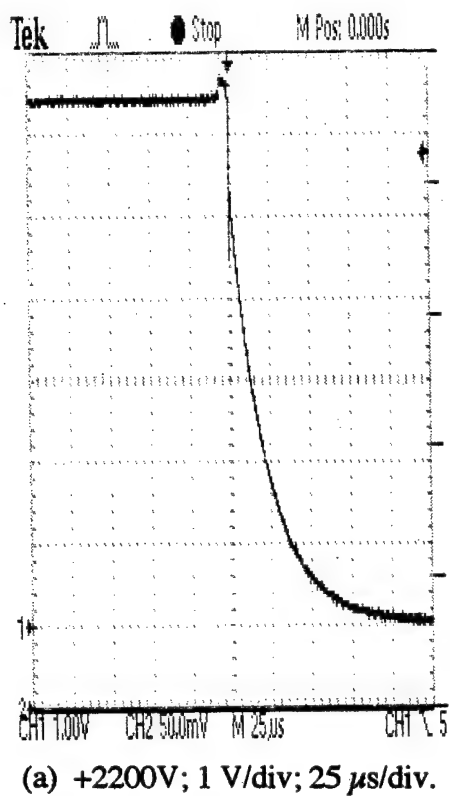

(c) +5400V; 2 V/div; 5 μs/div.

Fig. 10. TOF Waveforms of 3 nozzle designs(see Table 1)

4.2   Propellant System Emission Characterization

A brief review of the various modes of electrostatic spraying shows the capability of forming charged microclusters in the micro-dimension regime. Figure 11 summarizes the different stages of microcluster emission from capillary nozzles (typically 0.2 to 1mm O.D.) as successively higher voltages are applied to the emitter. The onset of charged

Increasing V →

Single-Cone   Intermediate   Crown Emission
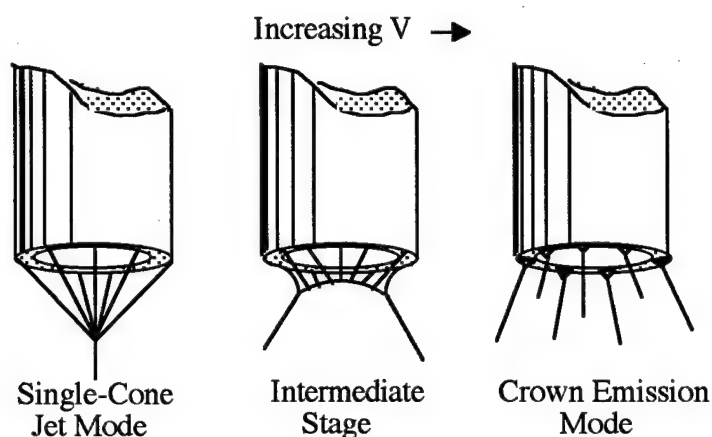Jet Mode   Stage   Mode

Fig. 11 Various stages of microcluster emission

cluster emission occurs when the conducting liquid is pulled into a Taylor cone configuration (single-cone jet mode) by electrostatic forces acting on the liquid. Increasing the nozzle potential above the onset voltage causes a transition from the single jet mode to a multiple jet mode (intermediate stage). At still higher applied voltages, the liquid meniscus retracts within the nozzle and charged cluster emission occurs from a plurality of micron-sized emission sites located on the capillary rim (crown emission mode). The existence of crown emission, characterized by the formation of multiple, cusplike structures, was first reported by Zeleny[3] in 1915. Photographs verifying the crown emission mode have been captured in optical studies of electrohydrodynamic (EHD) disintegration of liquids using 0.4 mm diameter nozzles[4].
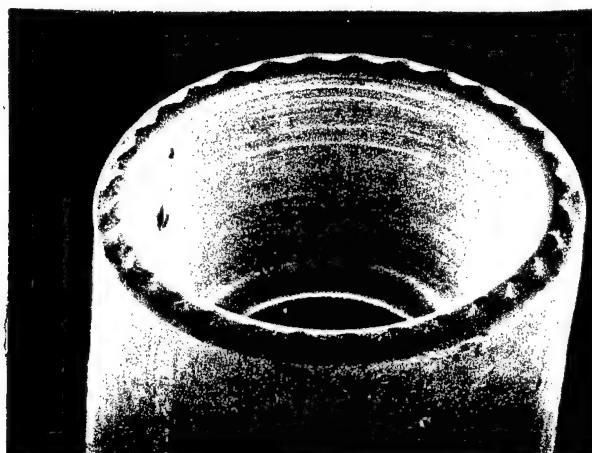
Fig. 12   SEM of capillary rim showing uniformly spaced emission sites (Zafran,1976)

10

A rather remarkable scanning electron microscope (SEM) photograph was published showing details of a capillary emitter lifetested to assess the reliability of components used in colloid space thrusters[5]. Fig. 12 reproduces the SEM photograph which shows details of a platinum capillary emitter tip (0.014 inches dia.) after 1875 hours of continuous operation in the crown emission mode. During the life test, the capillary was operated with a net extraction voltage of +14 kV at 9.5 μA emission current. The striking feature of the SEM is the scalloped pattern along the capillary rim. This confirms that a wave pattern was established in the liquid film by the applied electric field, producing an array of emissive sites, distributed around the rim periphery. The emitting sites form in a thin, wetting layer of liquid by the pulling action of electrostatic stress acting on the charged surface. The non-eroded plateau regions provide the "anchor" confining the multiple sites for emission of charged microclusters.

Compared to microfabrication capabilities, the capillary outer diameter (Fig. 12) is large ($\approx$ 350 microns), *but the characteristic dimension of a single emitter site is much smaller.* By letting λ represent the separation between emitter sites, the capillary tip geometry yields the following expression for the wavelength,

$$\lambda = 2\pi r / n \qquad\qquad (6)$$

where r is the capillary radius. Taking n = 32 (estimated from Fig.12) and r = 175 micron, $\lambda \approx 34$ micron indicating a characteristic site dimension (= λ/2) of 17 micron, an order of magnitude smaller than the capillary radius. This example, based on actual "macro" emission data, confirms that microcluster emission originates from sites having microstructural dimensions.

4.2.1 Emission Spray Pattern

To better understand the nature of the emission from a nozzle, it is useful to observe the spray pattern to estimate the emission profile. The spray pattern is attained by spraying directly onto a substrate for an extended period with higher potentials and visually inspecting any color changes. An aluminum plate was chosen as a suitable substrate for testing. Spraying with micro-cluster emission technology for approximately 20 minutes, a circular pattern with a gradient in the density is attained(Fig. 13). The pattern appears to be three concentric circles. From the center circle, is a dark discoloration(dark center) which is fairly uniform in density. The second circle is a ring with an even darker discoloration(heavy rim). The outer circle is a ring pattern with a shiny luster. This pattern indicates that emission density is the greatest around the rim of the nozzle. And most of the spraying is occurring within the rim, with some clusters from the rim spreading out of the circle. An estimated emission profile is seen on Fig. 14.
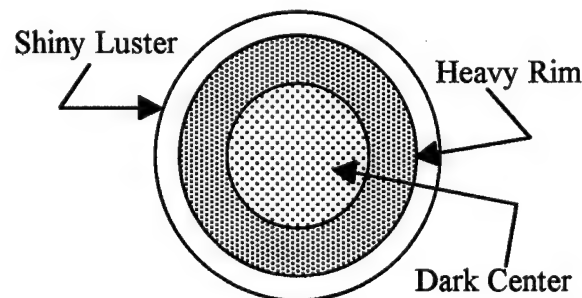

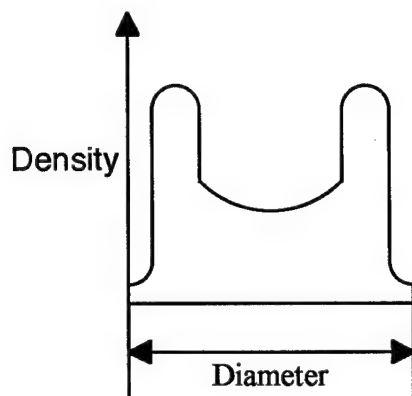Fig. 13 Pattern of emission of single emitter

11

Fig. 14 Estimated density profile of emission over the diameter of pattern

The pattern illustrated in Figs. 13 & 14 is only one of many patterns produced by micro-cluster emission, depending upon the operational emission parameters and the propellant fluid. Pattern measurements are used as a tool to study the emission modes and the dynamic activities that occur at the nozzle tip. Different patterns are a result of changes which occur at individual emission sites on the rim of a Micro-Capillary Tube emitter(Fig.15). As electric fields increase, the number of emission sites increase around the rim. The sum of the beams from all the emission sites form the spray patterns seen on the substrates. The effects of the overlapping of beams is discussed later.
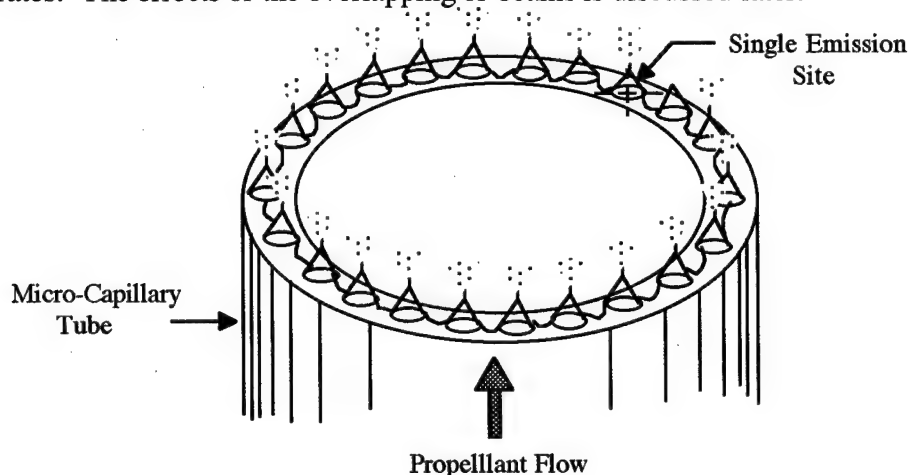

Fig. 15

Further studies showed the effects of current and flowrate to the average charge-to-mass ratio and the spray pattern. For visualization purposes, emitters must be operated at higher potentials and greater flowrates than the planned MEM's thruster operational conditions. This data can be used to determine trends in emission due to varying operating conditions.

First off, by keeping a constant flowrate, dV/dt, of $0.636\mu l/min(1.06 \times 10^{-8}$ kg/s), and applying a constant potential of +15KV, the molarity of ammonium acetate of the propellant was varied and observed for emission effects. As seen in Figure 16, different molarity propellants produce differences in density and size of the spray pattern.
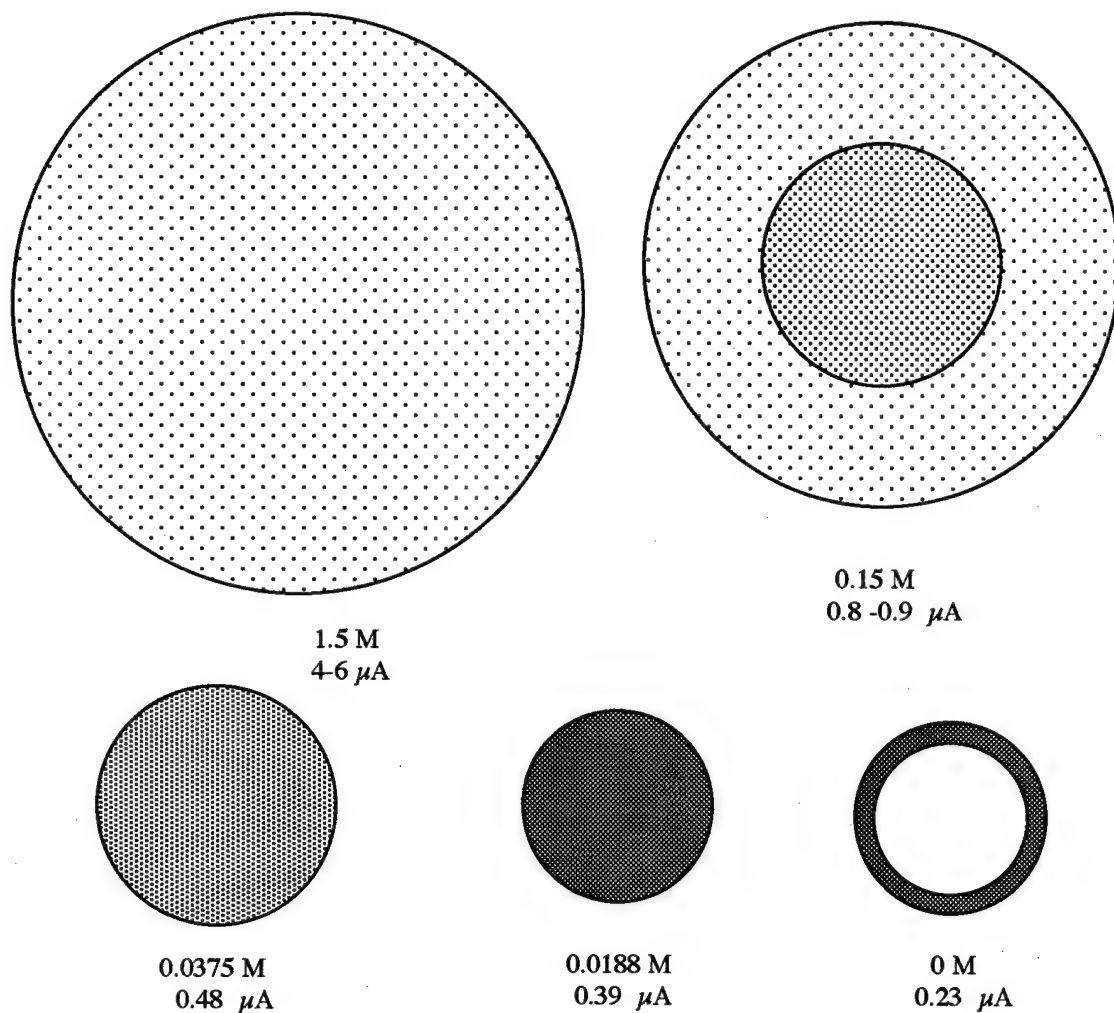
Fig. 16 All data at 15 kV. Substrate located ≈ 4.5" away and exposed to beam for 20 minutes. Flowrate ≈ 0.636 μl/min in all cases. (Circles to scale)

Molarity also affected the emission current by allowing greater amount of charge to be applied to the propellant. The increase in emission current results in a greater average charge-to-mass ratio. Along with greater q/m comes smaller microcluster sizes. This will be an important factor in increasing the specific impulse of an emitter.

Mol.	I (μA)	q/m (C/kg)	r (μ)	V (cm^3)	N (nucleons)	E (eV)	E/N (eV/N)
0	0.23	21.7	0.218	4.33×10^{-14}	2.59×10^{10}	8.87×10^{7}	0.0034
0.0188	0.39	36.8	0.153	1.50×10^{-14}	8.97×10^{9}	5.22×10^{7}	0.0058
0.0375	0.48	45.3	0.134	1.00×10^{-14}	5.98×10^{9}	4.28×10^{7}	0.0071
0.075	0.60	57.0	0.115	6.36×10^{-15}	3.80×10^{9}	3.40×10^{7}	0.0089
0.150	0.85	80.2	0.091	3.15×10^{-15}	1.88×10^{9}	2.40×10^{7}	0.0130
1.5	5.00	621.0	0.023	5.08×10^{-17}	3.04×10^{7}	3.04×10^{6}	0.100

Table 2

The currents and flowrate used to calculate values given in Table 2 were based on experimentally measured quantities. The remaining variables were calculated as follows:

a. The average charge-to-mass ratio q/m for microclusters were determined using the relationship

$$q/m = I/(dm/dt) \quad C/kg \tag{7}$$

where I is the emitter current (A), dm/dt is the mass flowrate (kg/s) and $dm/dt = \rho \, dV/dt$ (kg/s).

b. The microcluster radius r was calculated using a modified version of the Rayleigh criterion that estimates the most probable q/m as a function of particle radius given by

$$r = [2.08 \, (\varepsilon_0 \, \gamma)^{1/3}]/[\rho^{2/3} \, (q/m)^{2/3}] \tag{8}$$

where ε_0 is the permittivity of vacuum $= 8.85 \times 10^{-12}$ F/m, γ is the surface tension of the cluster solution taken as 0.062 N/m and ρ is the solution density assumed equal to 1.00×10^3 kg/m^3. Substitution of the above constants results in the reduced expression

$$r \approx 1.70 \times 10^{-6}/(q/m)^{2/3} \quad \text{meters} \tag{9}$$

c. The microcluster volume V, assumed spherical, is $4\pi r^3/3$.

d. The total number of nucleons in microclusters formed is computed from

$$N = \rho \, V/m_p \tag{10}$$

where ρ is the density of the microcluster solution and m_p is the proton mass.

e. The impact energy of microclusters on target substrates is $E = qV_a$ where q is the total net charge on the microcluster and V_a is the acceleration potential. Since q from the modified Rayleigh criterion is given by

$$q = 4\pi r^{3/2} (\varepsilon_0 \, \gamma)^{1/2} \tag{11}$$

the impact energy in electron volts becomes

$$E = [4\pi r^{3/2} (\varepsilon_0 \, \gamma)^{1/3} V_a]/e \quad eV \tag{12}$$

where e is the electronic charge. For $V_a = 15$ kV, the impact energy a function of microcluster radius reduces to

$$E = 8.72 \times 10^{17} \, r^{3/2} \tag{13}$$

From observing the patterns, the emission density increases as the current decreases. This is due to space charge effects of the emission microclusters. As microclusters increase in charge, the more quickly they repel each other causing them to spread out and decrease the pattern density. Without any propellant dopant, emission current 0.23 microamps is still detected. At this low current, the q/m is low enough to allow the microclusters to spray without much repulsion of each other. Without the space charge spreading, the pattern retains the ring shape of the emitter.

As currents increase, multi- density patterns result. As emission beams diverge, overlap of these beams from around the rim of the circular emitter causes the density gradient. This effect is illustrated in Fig. 17. In the case with 0.8 to 0.9 microamps, beams from opposite emission sites of an emitter overlap, causing a higher density where they overlap. The low density outer rim is a result of minimal overlap.
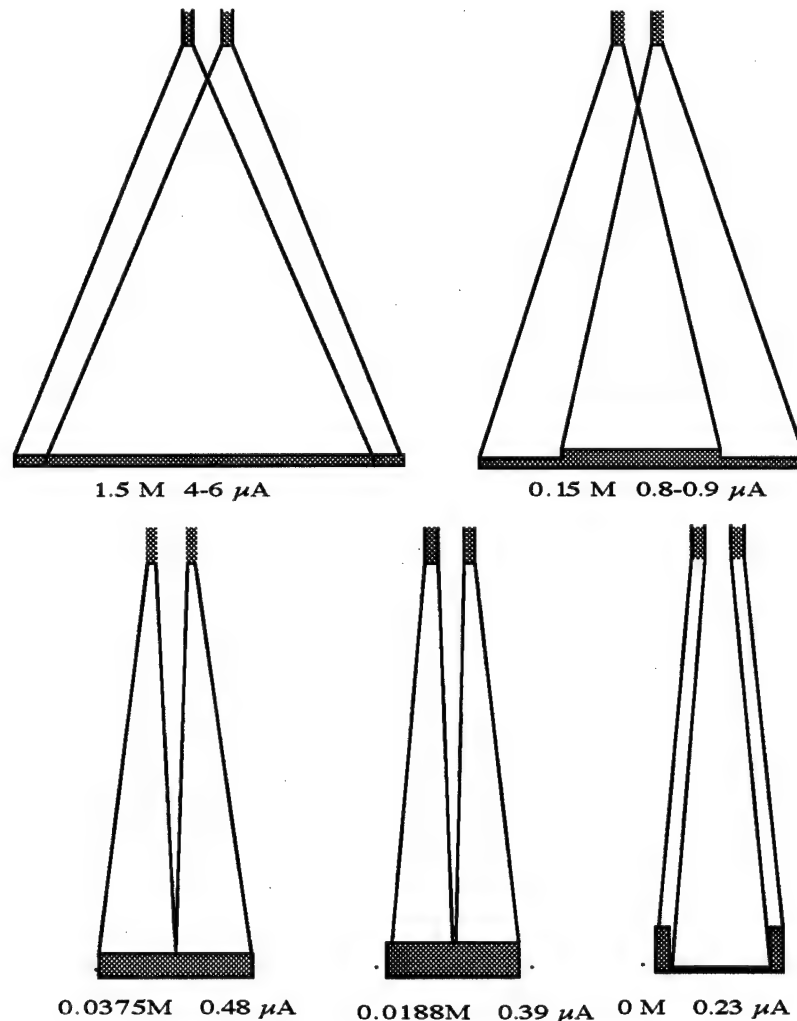

1.5 M   4-6 μA   0.15 M   0.8-0.9 μA

0.0375M   0.48 μA   0.0188M   0.39 μA   0 M   0.23 μA

Fig. 17

Having smaller particles due to higher <q/m> is beneficial in one sense, however the result of broader beams is a detriment. When the emission beam is broken down to its x and y coordinates, it can be seen that the thrust in the y direction is the only one producing the desired propulsion. The sum of vectors in the x direction($\Sigma Mx \approx 0$) provide no desired propulsion(Fig.18). Looking microscopically, each microcluster has an x and y energy vector(Fig.19). Energy in the x vector($M\cos\theta$) is useless for the desired propulsion. So, in order to maximize the thrust efficiency of each microcluster, the vector must be directed more in the y direction($M\sin\theta$) while keeping the same magnitude. This means that with energy being equal, narrower beams will produce greater thrust. This can be done by controlling the propellant flowrate.
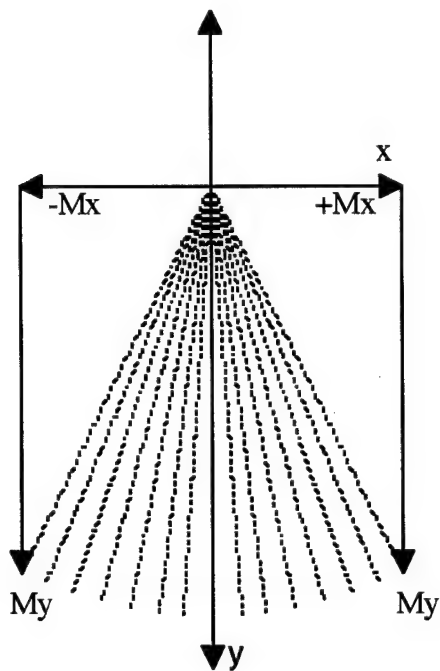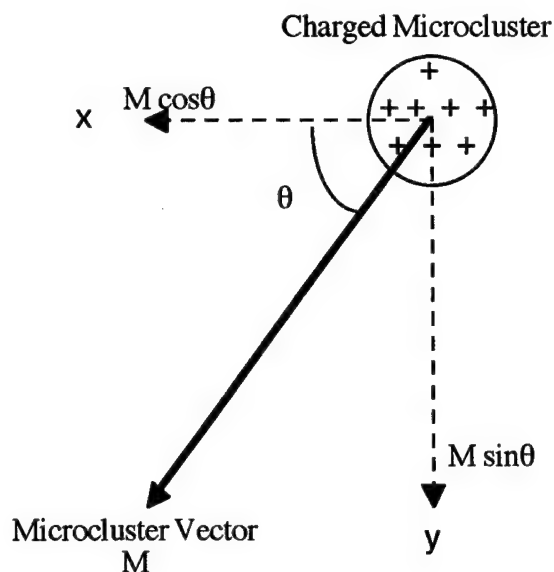
15

Fig. 18

Fig. 19

It was stated earlier that restricting the flowrate will allow for greater charge-to-mass ratios. This is shown by the results of emitting microcluster beams at different flowrates. Using a constant voltage of +15KV and a 0.0188M Ammonium Acetate solution as propellant, patterns similar to those in Fig. 20 were seen.

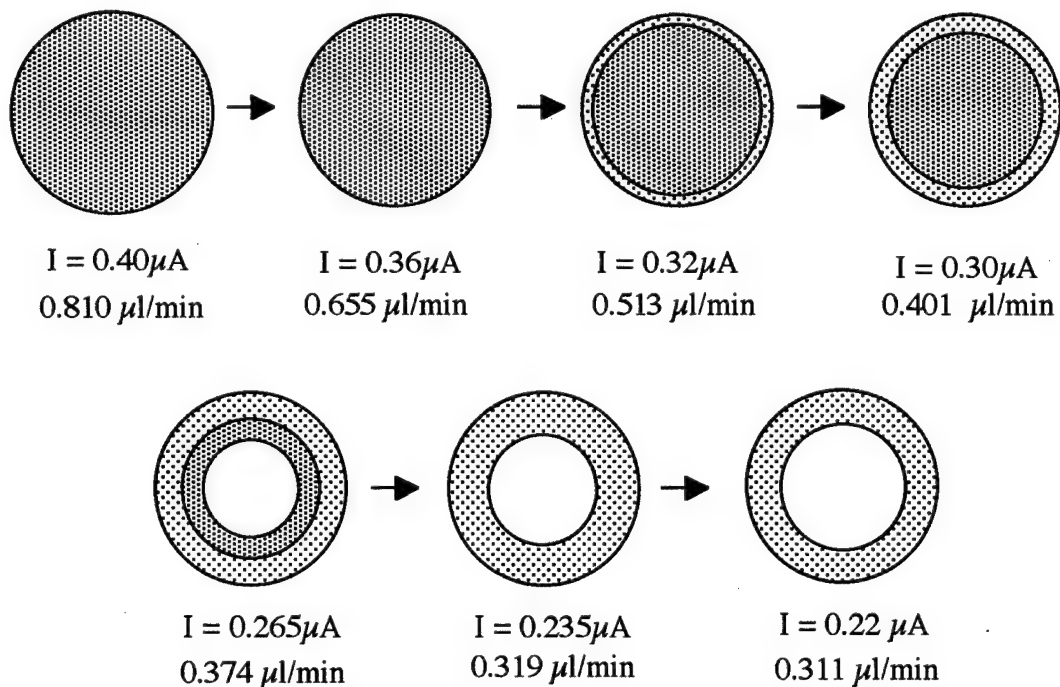| I = 0.40μA | I = 0.36μA | I = 0.32μA | I = 0.30μA |
| 0.810 μl/min | 0.655 μl/min | 0.513 μl/min | 0.401 μl/min |

| I = 0.265μA | I = 0.235μA | I = 0.22 μA |
| 0.374 μl/min | 0.319 μl/min | 0.311 μl/min |

Fig. 20

16

dV/dt (μl/min)	I (μA)	q/m (C/kg)	r (μ)
0.311	0.220	42.5	0.140
0.319	0.235	44.3	0.136
0.374	0.265	42.5	0.140
0.401	0.300	44.9	0.134
0.513	0.320	37.5	0.152
0.655	0.360	33.0	0.165
0.810	0.400	29.6	0.178

Table 3

The calculated results seen on Table 3 demonstrate the trend that lower flowrates lower emission current while raising the <q/m>. The patterns also indicate that restricting the flowrate can help in producing narrower emission beams for greater thrust.

This study can ultimately provide data necessary for development of long lifetime and reliable operation along with a wide range of thrust levels. To reach the desired levels of Specific Impulse and Thrust for micropropulsion, higher molarity and lower flowrates are needed.

4.2.2 Emission Spray Interaction

The actual propulsion system for nanosatellites will consist of an array for emitter nozzles on a MEM's chip. The array would place nozzles in close proximity of each other. This will lead to emission interaction from neighboring nozzles. The emission interaction was tested by spraying a 4 X 1 emitter array on an aluminum plate substrate. With all 4 emitters spraying simultaneously with positive voltage, an overlap of the emission beam occurred(Fig. 21). The individual circular patterns of each nozzle remained intact, while the areas of overlapping emission had an expected heavier density. This indicates that adjacent similar charged beams won't repel each other but rather have a cumulative effect down stream.
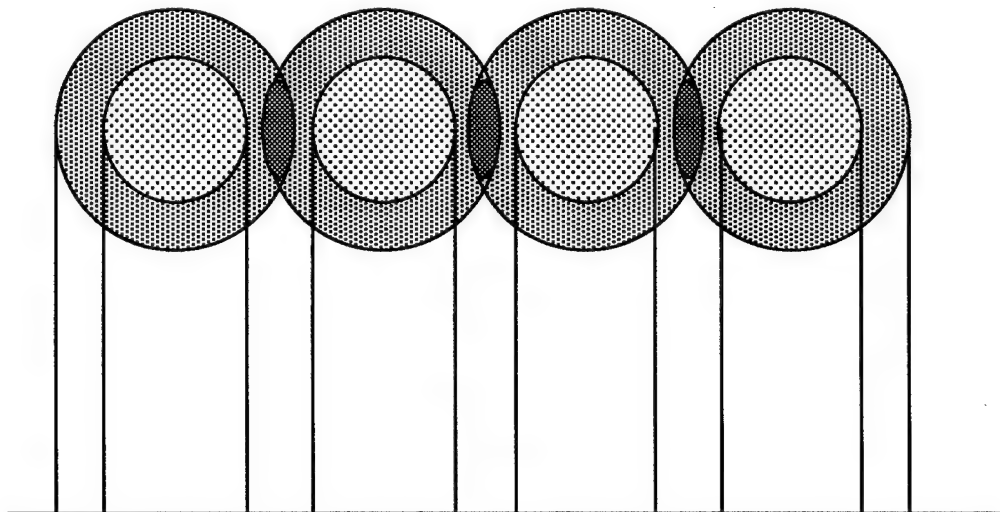

Fig. 21

17

4.3   DLTOF Velocimetry

While indirect measurements of thrust and specific impulse using TOF methods have been applied previously to the evaluation of the performance of colloid thrusters, the direct measurement of droplet velocities have not been previously reported. Such a measurement would be direct verification of the specific impulse. The typical velocities of interest (> 1000 m/s) is well beyond the capabilities of most modern particle velocity diagnostics such as particle image velocimetry and phase-Doppler velocimetry. In the Phase I effort, we evaluated the potential performance of a dual laser TOF velocity diagnostic.

In DLTOF velocimetry, two laser beams at visible wavelengths (preferably a helium-neon laser) are focused to their diffraction limit (a few microns in thickness), or, no more than 10 times this limit, with cylindrical optics to form two parallel sheets of light passing through the colloid droplet plume normal to the central jet axis (see Fig. 22). The sheet
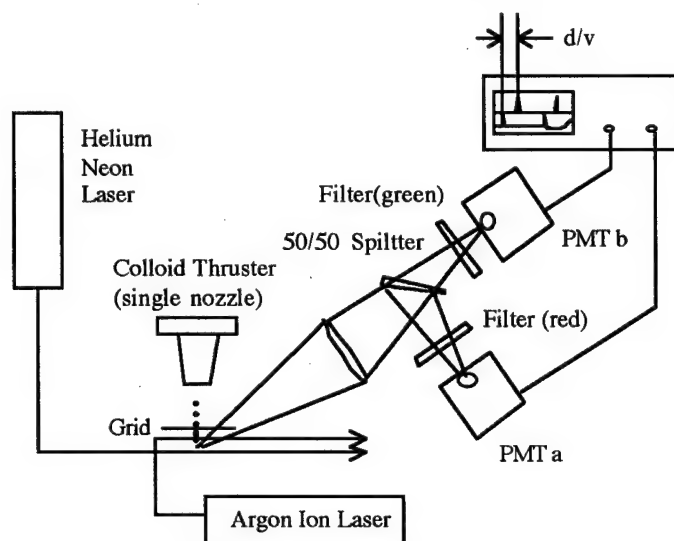

Fig. 22   Schematic of the experimental facility for DLTOF. Shown is the two color option.

separation is approximately d = 1 mm, which will set the spatial average over which accurate velocities can be obtained. As a droplet passes first through the top sheet, then at a time ≈ τ = d/v, through the bottom sheet, the droplet, through Mie scattering, scatters light into a solid angle, $d\Omega$, subtended by a collection lens which images the scattered light onto the active photocathode of a fast risetime (≈ 3ns) photomultiplier (PMT), as illustrated in Fig. 23. The successive PMT current pulses recorded in time register the time separation between the two events.   While many events can simultaneously take place (within a narrow time window) as the spatial collection volume is intentionally chosen to be sufficiently large to overlap with both intersection locations of a single droplet, an autocorrelation of the time-varying current will appropriately select the "pair events" from which the velocity can be extracted.
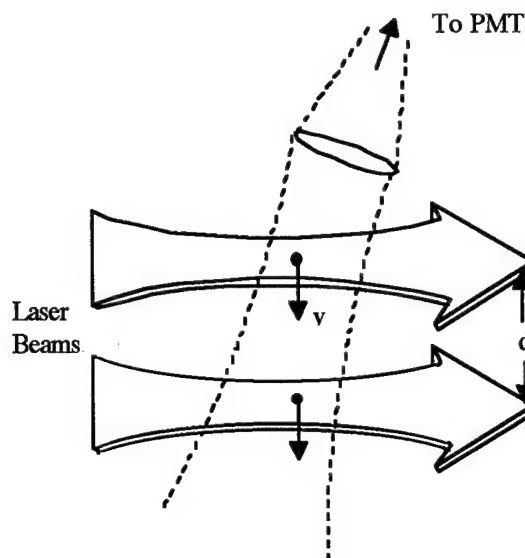
Fig. 23 Detailed schematic of particle-laser interaction volume.

A variation of this diagnostic can be used to ensure that the two successive signals recorded by a single drop is not confused with two recorded signals on one sheet from two droplets in succession. In this case, laser sheets of different wavelengths can be used along with two photomultipliers which are sensitized to scattering from a particular sheet through the use of narrow band interference filters. With this arrangement, scattering events from individual sheets are recorded on separate oscilloscope traces. The two traces can now be correlated to reveal the "pair events" corresponding to the passage of a single droplet across the sheet separation distance.

The success of this diagnostic depends critically on three factors: (a) that the assumption of Mie scattering is justified (particle size is no less than 1/10 of the laser wavelength used), (b) that there is a sufficient scattering intensity to register an analogue pulse at the anode of the photomultiplier, and (c) that there are at least one (and no more than 10) particles within the volume of the laser sheets imaged onto the photodetector at an instant in time. The Phase I effort included an evaluation of these restrictions.

The conclusions that are drawn from the Phase I study are straightforward. The DLTOF method is a viable method for measuring colloid particle velocities over a range of operating conditions of interest to thruster operation. However, the colloid thruster beam generated at the most optimum conditions of interest gives rise to conditions that are unsuitable for this diagnostic. The DLTOF, nonetheless, provides a means of checking the scaling laws over the broader range of particle emission, and a comparison to the less direct but more frequently used TOF methods.

The Phase I effort also included the initial fabrication of a demonstration experiment of the DLTOF method. The demonstration experiment consists of a single diode laser beam (630nm) shaped by a cylindrical lens of focal length 10 mm aligned to pass between the emitter of a single-emitter unit prototype colloid thruster fabricated during the Phase I study. Mie scattering off the colloid particles was collected at near-forward scattering geometries using a 5 cm diameter and 10 cm focal length lens.

4.4   Prototype Hardware Development

The Phase I study included the initial fabrication of a single-emitter and 100-emitter thrusters. Both the single and 100-emitter thrusters have 0.006-in OD/0.002-in bore stainless steel capillaries. The capillaries were soft-soldered to a brass holding plate, which is separated from the extractor plate by a predetermined distance (about 3 mm in its present configuration) by a boron nitride spacer. Propellant is introduced through a stainless steel fastener plate mounted to a Teflon propellant reservoir onto which the brass emitter assembly is attached. The design of the 100-emitter thruster is based in part on the prototype colloid thruster designed and fabricated by Zafran et al[6]. At present, propellant is gravity-fed through a storage reservoir and delivered via flexible clear polyvinyl tubing that is metered by introducing a small air bubble and following transport of this bubble during the firing process. Firing of the single-emitter in air with unseeded glycerol and a 3kV emitter-collector potential resulted in emission currents of 10-20 picoamperes at inferred flowrates of less than 10^{-10} kg/s.

The Phase I effort included the development of simulation of the expected field distribution and particle trajectories for aid in optimizing the geometry of the extractor and needle configuration. The simulation is based on the solution of the Poisson equation in the region between the extractor plate and the emitter, and between the extractor plate and the distant space. At present, the model does not account for the possible field perturbation die to the finite space charge associated with the non-zero particle densities in these regions. However, because of the low particle loading (10^{10}-10^{12} particles/m^3), this distortion is estimated to be small. The calculated fields are used to estimate the particle trajectories. The trajectory simulations place a particle with a known specific charge (determined from the empirical relations developed in Ref. 7) and a particle mass determined by applying the Rayleigh criterion at arbitrary positions along the edge of the source needle. The equation of motion of the particle is solved giving the particle position and particle velocity at any point in time. The trajectory results can be used to determine the specific impulse, which can be lower than that predicted simply on the basis of an applied potential and known specific charge, because of the possibility of particle capture on the extractor. The results of the calculations depend largely on the geometry of the emission surface (shape of the propellant meniscus) and the position-dependent emission rate that is used. A simplified calculation was performed which demonstrates the utility of this simulation. The results are depicted in Fig. 24. In this figure, we depict the emitter needle as the vertical rectangular element. The extractor is an apertured horizontal element, identified partially by the interrupted trajectories. The needle is maintained at a potential of +2kV over its entire surface (including that of the assumed horizontal meniscus), while the extractor is at a -1kV potential over its entire surface. All other surfaces (including the outside boundary beyond the extractor) are taken to be electrically floating, except the distant boundary parallel to the extractor which is taken to be at zero (ground) potential* . The lines show the particle trajectories for unseeded glycerol, assuming that particles are emitted with equal probabilities over the entire meniscus.

---

* Note that this latter condition relies on the assumption that the distant space potential is that of the satellite reference (i.e., the satellite is at a potential close to that of the surrounding space plasma), and that the presence of an extractor at a high negative potential does not greatly affect the distant space potential. In practice, a ground shield would be designed to provide a drift region of low electric field between the thruster and the distant space plasma.
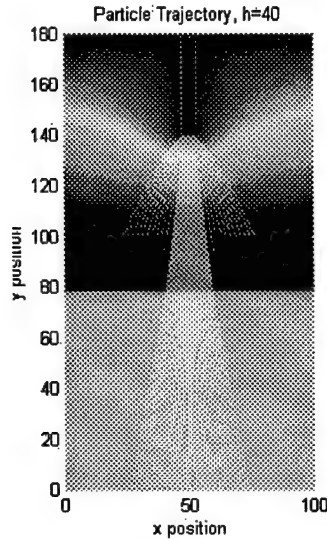
Fig. 24 Results of particle trajectory calculations for unseeded glycerol.

Although simplified, this calculation gives us significant insight into the particle transport problem. We see that some fraction (albeit small in this calculation) of the particles strike the extractor. On the other hand, the majority of the emitted particles pass through the orifice in the extractor and eventually escape the influence of the extractor potential. The axial particle velocity profile is shown in Figure 25. We see that the particles are accelerated to their maximum velocities at a point just before entering the extractor orifice. Inside the orifice, they drift with constant velocity, which is expected. Beyond the orifice, we find that the particles lose about 30% of their axial velocity, again an expected result, since the particles continue to experience the -1KV potential of the outside surface of the extractor. Within a very short distance, however, they decelerate to the escape velocity, which in this case, is roughly 2/3 the peak velocity in proportion to the ratio of the potentials on the needle and extractor. The trajectory calculations also indicate that optimization of the location and geometry of the emitter-extractor assembly can make additional improvements to the performance of the thruster. Phase II research and development would continue these calculations for higher conductivity propellants.
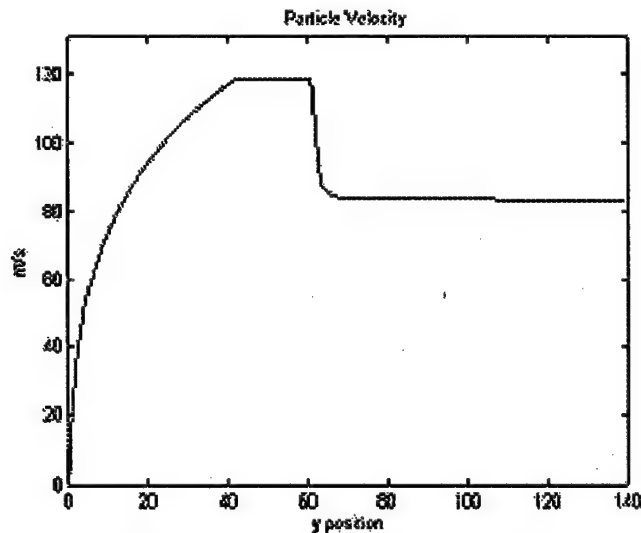

Fig. 25 Calculated center-line charged particle velocities for unseeded glycerol.

21

4.5   MEMS Design

Micro-cluster beams are now routinely generated by EHD liquid atomization from single capillary orifices with diameters ranging between about 1 - 100 microns. Thrust levels beyond that achievable with single emitters are produced by microfabricating arrays having multiple capillary orifices[8]. For a micro or nanosatellite configuration, a propulsion system is envisioned consisting of multiple emitters fabricated by MEMS (microelectromechanical systems) technology. Candidate materials and structural designs for batch-fabricating micro-cluster emitters using MEMS technology have been and will continue to be explored. These studies included the following microfabrication techniques for creating small orifice emitters:

a. Spindt microvolcanos or microtips

b. Anisotropic microetching of Si [9]

c. Microetched channels with anodic bonding

Spindt Microvolcanos or Microtips

Already technology for batch-fabricating such structures, known as Spindt microvolcanos, has been demonstrated at SRI International (Menlo Park, CA)[10]. Fig. 26 illustrates a cross-section of a microfabricated volcano emitter proposed for a micro-spacecraft thruster element. Eventually, monolithic arrays consisting of joint emitter and acceleration electrodes could be cast by evaporating metal onto insulating, oxide substrates.
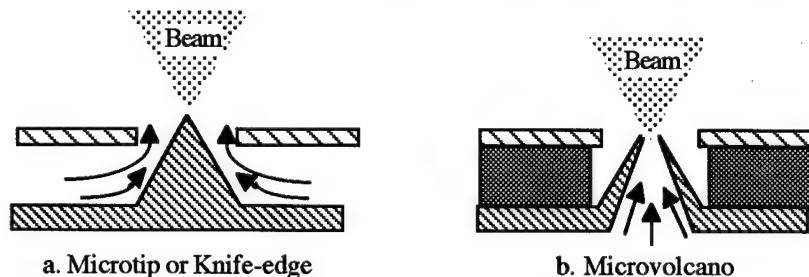

a. Microtip or Knife-edge   b. Microvolcano

Fig.26. Microcluster Emitter MEMS Configurations.

Micro-dimensions inherent in the MEMS devices depicted in Fig.26 potentially provide the necessary physical structures required to generate high specific impulse beams. The requirements placed on the microstructures are twofold: (1) the microflow channels must provide a high impedance to propellant flow ($\approx 10^{-12}$ kg/s) and (2) electric fields of the order $0.5\text{-}1.0 \times 10^6$ V/cm must be generated at the microtip apices or microvolcano exit orifices. Initial MEMS design specifications that meet the electric field requirement can be determined analytically. The electric field E at microtips can be approximated using[11]

$$E = 2V/r\ln(4x/r) \tag{14}$$

where r is the microtip/microvolcano apex dimension, V is the voltage applied to the microtip and x is the microtip/extractor electrode separation. Using this expression, operating voltages and microtip dimensions can be selected consistent with thruster performance and microfabrication limitations.

Anisotropic Microetching of Silicon

As depicted in Fig.27, anisotropic etching of (100) silicon can be used to fabricate micro-orifices in silicon wafers. In the figure W_m represents the silicon oxide mask opening used to expose the silicon to the etchant, W_o is the width of the rectangular or square cavity bottom plane and z is the etch depth. With a wall slope of $\theta = 54.74$ degrees, W_o, corresponding to the emitter micro-orifice is given by

$$W_o = W_m - 2z \cot\theta \qquad (15)$$

or

$$W_o = W_m - 2^{1/2} z \qquad (16)$$

If the mask opening is wide enough, the etched pit in the silicon will extend all the way through the substrate, creating a small orifice. Typically for $z = 600$ μm, $W_m > 849$ μm is required to fabricate micro-orifices in this manner.
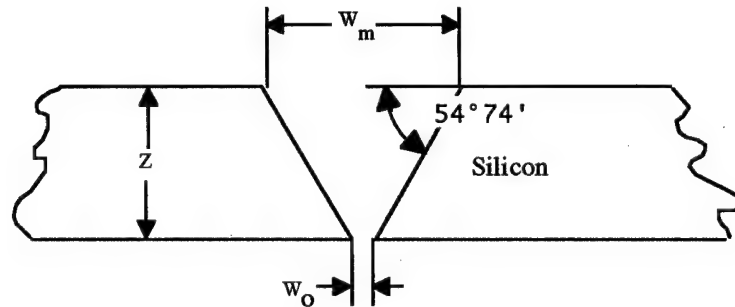

Fig.27 Anisotropic Etching of Silicon

Microetched Channels With Anodic Bonding

Another concept for microfabricating multiple, micro-cluster emitter orifices involves anisotropically etched grooves in a silicon wafer for producing end-orifices and microflow channels. This concept
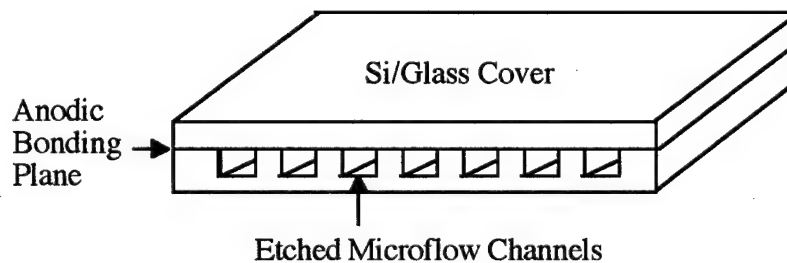

Fig. 28 Etched Microchannels with anodically bonded enclosure

is illustrated in Fig.28. The microflow channels can be enclosed by anodically bonding a silicon or glass cover plate to seal the microfabricated unit.

After evaluating many of the most applicable micromanufacturing methods and the findings from the research conducted from this and previous program, the following MEMS designs were recommend as tasks for further study under a Phase II program for nanosatellite propulsion technology.

4.5.1 MEMS Design of Single Emitter Microthruster

Before undertaking the more difficult and extensive task of micromachining multiple emitter arrays, it is important to explore the characteristic performance of a single, micromachined emitter. The final design of a single MEMS emitter will be completed after reviewing various approaches to the micromachining details submitted by qualified facilities based on PSI's specifications. We will conduct a systematic survey of facilities (including federally funded, educational and commercial institutions) with the capability and previous experience of microfabricating related device structures.

The preliminary, micromachined emitter test assembly has been designed to include the functional elements depicted in Fig. 29. The micromachined emitter element (denoted by the dashed box in the figure) will be integrated into a "macro" support structure consisting
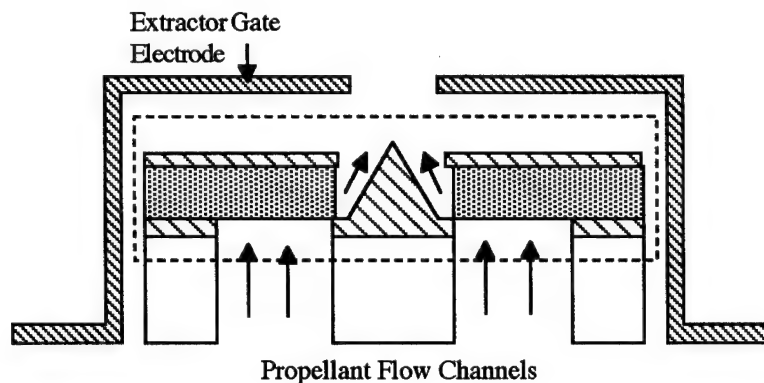

Fig.29 Micro-Emitter Hybrid Test Structure.

of an extractor electrode and a means for delivering the propellant fluid to the microtip. The more important issues to be addressed during the continued design stage of the hybrid test stand include: (1) the selection of microtip base material (silicon or metallic) and (2) the "macrofabrication" of preformed propellant flow channels in the microtip base material (before micromachining) for attaching "macro" flow connections. This testing is expected to provide crucial information with respect to wetting problems and thruster performance before undertaking MEMS fabricated array designs.

4.5.2 MEMS Design of Multiple-Emitter Arrays

Research on the Phase I program has led to the formulation of several design concepts for achieving the desired microelectric propulsion performance goals. Based on proven microfabrication methodologies, we propose to design micro-emitter array geometries that exploit the microfabrication techniques used for the development of electron field emission emitter arrays (FEAs). The structure of a liquid propellant microthruster array can be similar to FEAs by confining the liquid cusp to a region defined by the electron emitting

24

micromachined structure basic to FEA design. An example of a FEA device which can be modified to fit the proposed concept is given in Fig. 30 which shows a Spindt cathode array schematic. Details concerning the fabrication procedure for this type of array is given in a reference by Spidnt, Holland, Rosengreen, and Brodie[12].
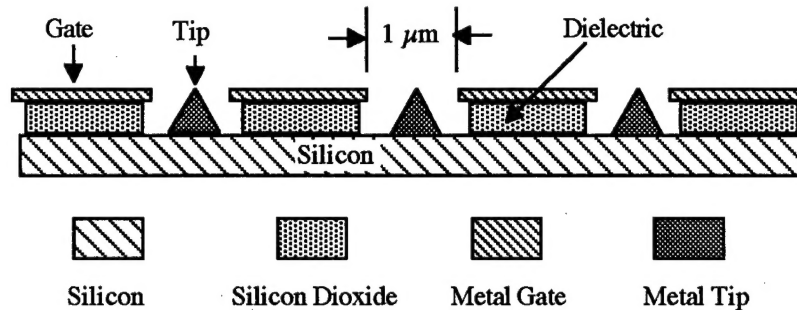

Fig. 30   Spindt Cathode Emitter Array.

Other examples of suitable fabrication procedures for micromachining FEA structures can be found in references 13-20. Typically, fields at the electron emitting tips of FEAs are of the order 5×10^7 V/cm with applied voltages less than 100 V. Note this is several orders of magnitude higher than the fields required to produce high specific impulse beams using charged microcluster emission.

The electrical connections for electron emissive operation of the Spindt array are shown in Fig. 31. Here, the emitter base is grounded and positive voltage is applied to the gate. Building on this FEA concept, a modified version for forming microcluster beams from conducting liquids is illustrated in Fig. 32. This microcluster triode arrangement, although
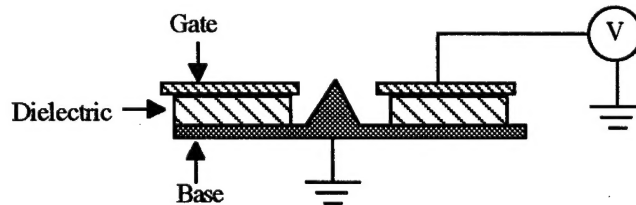

Fig. 31   Electrical Connections for Spindt Diode FEA Array.

similar to FEAs, has some significant structural and electrical modifications. First, the gate and emitter base are electrically connected in common. This common connection serves to (1) prevent liquid from electrically shorting to the gate (had it been grounded as in the Spindt diode case) and (2) guarantees the highest electric field remains a the emitter apex - unlike the case for cylindrical capillary emitters where the highest electric field exists at the capillary rim.
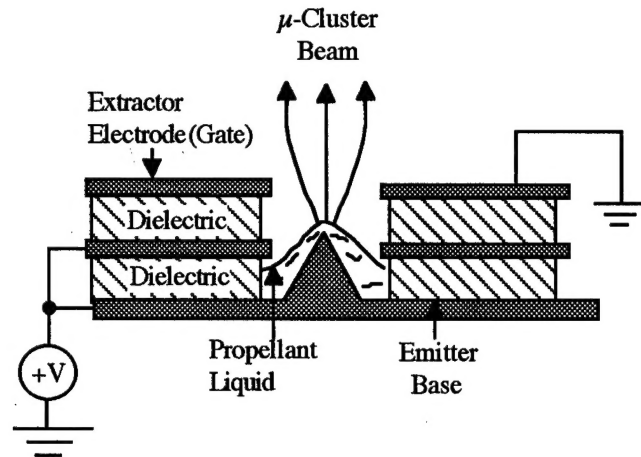
Fig. 32 Proposed Triode Microcluster Emitter Array.

Next, the microcluster emitter array has a triode structure. The function of the additional (grounded) extractor electrode, similar to the gate electrode in the Spindt diode array, is to aid in establishing a high field at the microcluster emitting apex. Although the extractor electrode is shown as separated by a dielectric material, a vacuum gap is preferable. Not shown in Fig. 32 is a means for feeding propellant liquid to the apex region. Propellant can be introduced from the rear of the triode structure via micromachined holes in the emitter base or laterally by means of grooves micromachined in the emitter base.

4.5.3 Knife-Edge Versus Point Source Microthruster Arrays

A novel approach for a microthruster design which does not rely on "point sources" for emitting structures will be examined on Phase II. This approach is based on previously reported work demonstrating the feasibility of microfabricating "knife-edge" electron field emission arrays[21]. This design, shown schematically in Fig. 33 has an obvious advantage
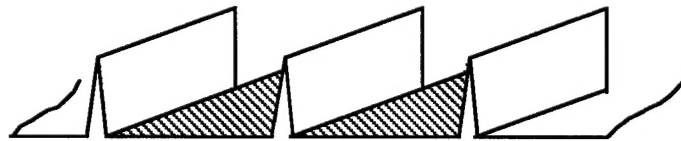

Fig. 33 Knife-Edge FEA Array (Gate Electrode Not Shown).

over point sources by reducing the number of micromachined structures necessary to achieve equivalent thrust levels. It may also alleviate the tolerances placed on lithography patterns compared to that required to microfabricate point sources. The number of microcluster emitting sites on the knife-edge will be determined by the electric field at the knife-edges and space charge effects. The distance between two adjacent emitting sites will be much smaller than what can be achieved using point source structures. The "knife-edge" approach could lead to more compact array structures, hence less weight, and more economical to produce than "point source" arrays.

These preliminary MEMS designs, contingent upon the results acquired from further study done on the Phase II portion of the project, will build naturally upon the future results

which will provide the fundamental insights for identifying multiple emitter array design specifications.

5.0   Work In Progress

Research in this area is continuing through Phrasor corresponding with Jet Propulsion Laboratory and Stanford University.   A Phase II proposal has been completed and submitted for review.

References

1   S.W. Janson and H. Helvajian, "Batch-Fabricated Microthrusters: Initial Results" AIAA paper 96-2988, 32nd AIAA/ASME/SAE/ASEE Joint Propulsion Conference, Lake Buena Vista, FL, July 1-3, 1996.

2   J. Mueller, "Thruster Options for Microspacecraft: A Review and Evaluation of Existing Hardware and Emerging Technologies", AIAA Paper 97-3058, 33rd AIAA/ASME/SAE/ASEE Joint Propulsion Conference, Seattle, WA., July 6-9, 1997.

3   J. Zeleny, "On the Condition of Instability of Electrified Drops With Applications to the Electrical Discharge From Liquid Points", Proc. Camb. Phil. Soc., **18**, 71 (1915).

4   U. Luttgens, Th. Dulcks and F.W. Rollgen, "Field Induced Disintegration of Glycerol Solutions Under Vacuum and Atmospheric Pressure Conditions Studied By Optical Microscopy and Mass Spectrometry", Surface Sci., 266, 197 (1992).

5   S. Zafran, Ed., *Colloid Advanced Development Program.* Tech. Report AFRPL-TR-76-19 (1976).

6   S. Zafran, J.C. Benyon and P.W. Kidd, AIAA 75-392, 11th Electrical Propulsion Conference, New Orleans, LA., March, 1975.

7   R.J. Pfeifer, C.D. Hendricks, Jr., AIAA Journal, 6, 496, 1968.

8   "Micro-Electric Propulsion Technology," SBIR Program with NASA Marshall Space Flight Center, duration, April 10 - Oct. 9, 1998.

9   M. Madou, "Fundamentals of Microfabrication," CRC Press, New York, 1997

10   C.A. Spindt, "Microfabricated Field-Emission and Field-Ionization Sources", Surf. Sci., **266**, 145 (1992).

11   R. Gomer, *Field Emission and Field Ionization*, Harvard University Press, Cambridge, MA., 1961.

12   C.A. Spindt, C.E. Holland, A. Rosengreen and I. Brodie, " Field-Emitter-Array Development For High Frequency Operation", J. Vac. Sci. Technol.B, 11, 468 (1993).

13   Q.Li, M.Y. Yuan, W.P. Kang, S.H. Tang, J.F. Xu, D. Zhang and J.L. Wu, "Fabrication and Characterization of Silicon Field Emission Diodes and Triodes", J. Vac. Sci. Technol.B, 12, 676 (1994).

14   D.Temple, W.D. Palmer, L.N. Yadon, J.E. Mancusi, D. Vellenga and G.E. McGuire, " Silicon Field Emitter Cathodes: Fabrication, Performance and Applications", J. Vac. Sci. Technol.A, 16, 1980 (1998).

15   M.R. Rakhshandehroo and S.W. Pang, "Fabrication of Self-aligned Silicon Field Emission Devices and Effects of Surface Passivation on Emission Current", J. Vac. Sci. Technol.B, 16, 765 (1998).

16   S.E. Huq, M. Huang, P.R. Wilshaw and P.D. Prewett, "Microfabrication and Characterization of Gridded Polycrystalline Silicon Field Emitter Devices", J. Vac. Sci. Technol.B, 16, 796 (1998).

17   J.R. Jessing, H.R. Kim, D.L. Parker and M.H. Weichold, " Fabrication and Characterization of Gated Porous Silicon Cathode Field Emission Arrays", J. Vac. Sci. Technol.B, 16, 777 (1998).

18   C.A. Spindt, C.E. Holland, P.R. Schwoebel and I. Brodie, " Field Emitter Array Development For Microwave Applications.II", J. Vac. Sci. Technol.B, 16, 758 (1998).

19   J.H. Lee, S.W. Kang, Y-H, Song, K.I. Cho, S.Y. Lee, and H.J. Yoo, " Fabrication and Characterization of Silicon Field Emitter Arrays by Spin-on-glass Etch-back Process", J. Vac. Sci. Technol.B, 16, 238 (1998).

20   S.W. Kang, J.H. Lee, B.G. Yu, K-I, Cho and H.Y. Yoo, " Novel Structure of a Silicon Cathode With a Sputtered TiW Gate Electrode", J. Vac. Sci. Technol.B, 16, 242 (1998).

21   B.Lee, T.S. Elliott, T.K. Mazumdar, P.M. McIntyre, Y. Pang, and H.-J. Trost, " Knife-Edge Thin Film Filed Emission Cathodes on (110) Silicon Wafers", J. Vac. Sci. Technol.B, 12, 644 (1994).